Phase Saturation Control on Vorticity Enhances Mixing in Porous Media

Journal Article

Author(s):
Velásquez-Parra, Andrés; Marone, Federica; Kaufmann, Rolf; Griffa, Michele; Jimenez-Martinez, Joaquin (iD)

Phase Saturation Control on Vorticity Enhances Mixing in Porous Media

Andrés Velásquez-Parra[1,2] , Federica Marone[3], Rolf Kaufmann[4,5] , Michele Griffa[4] , and Joaquín Jiménez-Martínez[1,2]

[1]Department of Water Resources and Drinking Water, Swiss Federal Institute of Aquatic Science and Technology, Eawag, Dübendorf, Switzerland, [2]Department of Civil, Environmental and Geomatic Engineering, ETH Zürich, Zürich, Switzerland, [3]Swiss Light Source, Paul Scherrer Institute, PSI, Villigen, Switzerland, [4]Swiss Federal Laboratories for Materials Science and Technology, Empa, Dübendorf, Switzerland, [5]Effectum Medical AG, Olten, Switzerland

Abstract Mixing controls the fate of any solute entering porous media. Hence, an understanding of the involved processes is essential for assessing subsurface contamination and planning for its protection. However, the three-dimensional mechanisms dominating solute mixing in the presence of several fluid phases in the pore space, and their dependency on phase saturation degree (fraction of the pore volume occupied by a phase) are unknown. Here, we analyze solute mixing in unsaturated porous media at the pore scale using X-ray micro-tomography performed with synchrotron radiation at unprecedented temporal and spatial resolutions for such an investigation. Transport experiments through a synthetic, sand-like porous medium, followed in 4D using a contrast solution, are performed at different liquid phase saturation degrees. The results reveal larger solute's front deformation at lower saturation, which translates into an enhanced mixing with time. Using different topological indexes, defined based on a description of the liquid phase geometry and of the resulting hydrodynamics, we show an increase in the spatial convergence of flow streamlines at lower saturation, which, in turn, leads to a strengthened helical flow inside the liquid phase. Consequently, this increases the number of shear- and vorticity-dominated deformation regions, as characterized by larger negative and positive Q-criterion values, respectively. These findings represent a major step toward understanding the control of both saturation and the system's heterogeneity on solute mixing, essential, among others, to assess reactivity in porous media.

Plain Language Summary The fate of any solute spreading through porous media, as it is the case for nutrients or pollutants entering the subsoil, is controlled by liquid-liquid mixing with the resident solution. However, it is still unknown which mechanisms control mixing in the presence of several fluid phases, as it occurs in the unsaturated region of soils. A combination of synchrotron 4D X-ray micro-tomography experiments with very high temporal and spatial resolutions, advanced 3D image analysis, and numerical simulations of flow, allowed to reveal an enhancement of the spatial convergence of flow streamlines at lower liquid phase content, that is, at a lower fraction of the entire pore volume that is occupied by the liquid phase. This increases the number of shear- and vorticity-dominated flow regions, inducing an overall larger solute front deformation with time and rendering mixing more efficient. These findings can highly contribute to the assessment of mixing and reactions in natural porous media.

1. Introduction

Porous media in the environment often include several material phases within the pore space, both in liquid and gas form. In such a case, porous media are commonly referred to as unsaturated. Subsurface examples include soils, which act as a filter and buffer for contaminants (Burauel & Baßmann, 2005), so as deep aquifers and exhausted hydrocarbon reservoirs, where geological sequestration of CO_2 is typically carried out (Szulczewski et al., 2012). In all these cases, flow and transport processes intrinsically occur at the micro-scale, within the liquid- or gas-filled voids (pores) between solid grains, whose size usually spans the range of a couple to hundreds of micrometers. In those locations, initially segregated miscible phases come into contact with each other and homogenize by the action of molecular diffusion through what is commonly referred to as mixing, increasing the volume occupied by the solute and smoothing out concentration gradients across their interface (Danckwerts, 1952; Kitanidis, 1994; Ottino, 1989). However, our current understanding of the micro-scale coupling of flow dynamics and associated liquid-liquid mixing and reactive processes in unsaturated porous media is very limited, owing to both the complexities related to the presence of multiple phases and the difficulty in

experimentally probing/observing these systems in real-time, in particular with visible light. The classical modeling approaches for solute transport in unsaturated porous media are often based on equivalent parameters (permeability, dispersion) derived from analogy with saturated conditions and on systematic ad hoc incorporation of a dependency on the phase saturation degree (the fraction of the pore volume occupied by a phase) (Simunek et al., 2008). However, expressing solute transport in terms of a bulk phase saturation value introduces inaccuracy due to the high degree of heterogeneity in these systems. Fundamentally, current large-scale (continuum) models (Simunek et al., 2008) cannot accurately predict the fate of chemicals and reactions (both liquid–liquid and liquid–solid) in unsaturated porous media because of the control exerted by pore-scale processes on mixing (Dentz et al., 2011; Li et al., 2017; Valdés et al., 2022).

Recent studies have attempted to identify and include the effect of this heterogeneity on flow and transport prediction across scales (Lasseux et al., 2021). 2D studies, mainly based on microfluidics experiments and pore-scale numerical simulations, have exposed signs of anomalous transport already in simplified, model system porous media (Bordoloi et al., 2022). Anomalous transport is usually characterized by breakthrough curves, that is, time series of the solute concentration at a fixed location, that show early arrival and long tailing, describing non-symmetric solute's plume spreading patterns and non-Fickian evolution of mixing in time (Berkowitz et al., 2006; de Anna et al., 2013, 2014; Levy & Berkowitz, 2003). Such behavior has been shown to be enhanced in unsaturated conditions (Hasan et al., 2019; Jiménez-Martínez et al., 2015, 2017; Karadimitriou et al., 2016), given the increase in the system's heterogeneity, that is, broader fluid flow velocity distributions (Velásquez-Parra et al., 2022). In particular, the presence of a second immiscible material phase in the pore space leads to both the formation of larger interface areas between mixing fluids and enhanced concentration gradients across them, rendering mixing more efficient (Jiménez-Martínez et al., 2015). New advances in imaging techniques such as magnetic resonance imaging (Lehoux et al., 2016; Markale et al., 2021), high-resolution laser imaging (Heyman et al., 2020), and X-ray micro-tomography (Boon et al., 2017; Hasan et al., 2020) have allowed expanding these observations to 3D systems, involving both artificial and real porous media. Advances in X-ray micro-tomography have increasingly enabled the imaging of rock- and soil-like samples and of flow and transport through them, both for real-time visualization of the physical processes themselves (Armstrong et al., 2016; Chen et al., 2021; Dobson et al., 2016; Hasan et al., 2020; Schlüter et al., 2016) and for supporting the development and validation of respective numerical investigations (Guédon et al., 2019; Kang et al., 2014; Puyguiraud et al., 2021; Shih et al., 2022). These studies have unveiled important features of pore-scale flow and transport, such as intermittency of local velocities and accelerations, essential to be taken into account for improved model formulations (Kang et al., 2014). They have also provided relevant findings on the mechanisms behind non-Fickian scalings both of plume spreading over time (Puyguiraud et al., 2021) and of pore-scale concentration distributions (Hasan et al., 2020). Such studies exemplify the potential of X-ray micro-tomography for flow and transport analyses. However, its use to study systematically similar processes in unsaturated porous media, at the pore scale, has not been fully explored yet. In particular, the control of saturation on solute plume deformation, as a driver of mixing, under nature-like conditions, remains an open question.

Under fully saturated conditions, 3D experimental studies at the Darcy scale have exposed the role of secondary flow motions, that is, helical flow, on mixing enhancement (Chiogna et al., 2016). Twisted streamlines strongly deform the solute plume, increasing the surface for diffusive mass transport and enhancing plume dilution (Chiogna et al., 2016; Yu et al., 2015). Studies in 2D heterogeneous flow fields have highlighted the interplay of vorticity- and shear-dominated deformation areas in bending the solute plume and enhancing plume dilution, respectively (de Barros et al., 2012). In these cases, topological indicators such as helicity density, reflecting the effect of vorticity on streamlines deformation, and indexes such as the Okubo-Weiss parameter (Okubo, 1970; Weiss, 1991) or the Q-criterion (Hunt et al., 1988), which can be used for characterizing both vorticity- and shear-dominated deformation regions, have been applied with success in mixing analyses. On the contrary, similar studies under unsaturated conditions have mainly drawn attention toward changes in the connectivity of the non-wetting phase during cycles of imbibition and drainage (Schlüter et al., 2016; Shih et al., 2022), and also during stages of constant saturation as a result of coalescence and snap-off events of trapped ganglia (Armstrong et al., 2016). The impact of saturation on wetting phase topology both in 2D and 3D model systems and its implications for flow and transport at the pore scale remain unanswered.

Here, we report a synergetic experimental and numerical 3D time-resolved (i.e., 4D) investigation and analysis of pore-scale solute mixing in unsaturated porous media. We show that lower saturation increases the spatial convergence of flow streamlines, allowing distant parcels of fluid to meet further downstream. This enhanced

streamlines convergence leads to a strengthened helical flow, enhancing both shear- and vorticity-dominated flow deformation regions. We took advantage of synchrotron radiation-based X-ray micro-tomography experiments, performed with temporal and spatial resolutions unprecedented for such an investigation, to image in 4D a solute's concentration field. Such high resolutions, together with extensive 3D image analysis approaches, have allowed us to characterize the liquid phase topology and its effect on the system's hydrodynamics. Thus, we could systematically study the impact of liquid phase saturation and of fluid flow rates on mixing. Our results reveal that not only the bulk liquid phase saturation, but also its impact on both liquid phase topology and streamlines convergence, is fundamental for understanding and predicting the dynamics of contaminants and of geochemical cycles in soils.

2. Methods

2.1. Synchrotron X-Ray Micro-Tomography Experiments

Results obtained from 4D synchrotron X-ray micro-tomography performed during transport experiments allowed the observation of real-time concentration changes inside the pore space of a soil-like sample, under different saturation degrees ($S_w = V_w/V_T$, where V_w is the volume occupied by the liquid phase and V_T is the total pore space volume). Experiments were carried out at the beamline for Tomographic Microscopy and Coherent Radiology Experiments (TOMCAT) of the Swiss Light Source (SLS), located at the Paul Scherrer Institute (PSI), in Villigen, Switzerland. An artificial porous system, consisting of a sintered packing of irregularly shaped borosilicate glass grains (Hilgenberg GmbH), was used for all transport experiments. The cylindrical sample was 8 mm high and had a diameter of 4 mm, with a bulk porosity of 0.28, an intrinsic permeability of 10^{-10} m^2, and an average pore size of 30 μm. It resembled a poorly graded sandy soil, with a relatively homogeneous pore size distribution (refer to Figure S1 in the Supporting Information S1 for the pore size distribution) and close to a spatial constant porosity. This represents a more realistic porous medium than the simplified porous systems consisting of spherical glass beads, usually employed in similar transport studies (Hasan et al., 2020; Heyman et al., 2020). A 3D rendering of the porous system's tomographic reconstruction together with the air phase hosted inside of the pore space is shown in Figure 1a for the experiment performed at a saturation degree $S_w = 0.82$.

The sample was placed inside a flow cell composed of three units: (a) a bottom conic cap allowing the separate and simultaneous injection of both the liquid and the gas (air) phases, (b) a middle cylindrical casing, hosting the sample, and (c) a top conic cap allowing the connection of the outlet line. The middle casing was internally coated with paraffin to avoid lateral flow and boundary effects. We fabricated each unit via 3D printing by stereolithography, using a photosensitive resin composed of acrylic monomers. The same pair of sample and flow cell was employed for all transport experiments. The pressure was constantly monitored during the experiments via two sensors (MPS by Elveflow) placed at the end of the inlet and outlet lines, respectively. A potassium iodine (KI) aqueous solution was used both as a tracer and as background, that is, resident solution, albeit at different concentrations, namely, 0.06 M for the resident solution and 0.90 M for the injected tracer. The use of KI is justified in its lack of chemical reactivity with borosilicate glass and its high effective atomic number. This resulted in an optimal trade-off between X-ray absorption and phase contrast levels both between such a solution and air and between such a solution and the grain packing (Marone et al., 2020).

In the first stage, a simultaneous injection of both the gas (air) and the liquid phase (the aqueous solution) was performed until reaching a steady-state flow condition within the sample, that is, until no large oscillations in the pressure difference between the inlet and outlet were registered. Then, the fluid pair injection was stopped, resulting in a static mixture of the two phases (Tallakstad, Knudsen, et al., 2009). The injection was performed with an automatically controlled syringe pump (Harvard Apparatus) at a constant flow rate. Transport experiments were carried out in a second stage with the goal of observing, in real-time, the impact of both S_w and the flow rate, q, on solute transport and mixing. The tested flow rates included 0.125, 0.25, and 0.50 mm^3 s^{-1}. We injected the tracer at low capillary numbers (ratio between viscous and capillary forces) to guarantee that the air (non-wetting phase) remained immobile during the tracer injection (Tallakstad, Løvoll, et al., 2009; Tang et al., 2019). We estimated an average (across experiments) capillary number $C_a = 2.67 \times 10^{-6}$, here defined as $C_a = \bar{v}\mu/\sigma$, where $\bar{v}$ is the average flow velocity associated with every experiment and obtained through numerical simulations of flow, and μ and σ are the average dynamic viscosity, that is, 8.65×10^{-4} kg m^{-1} s^{-1} (Desnoyers & Perron, 1972), and the average surface tension, that is, 72.5 mN m^{-1} (Ali et al., 2009), of the KI
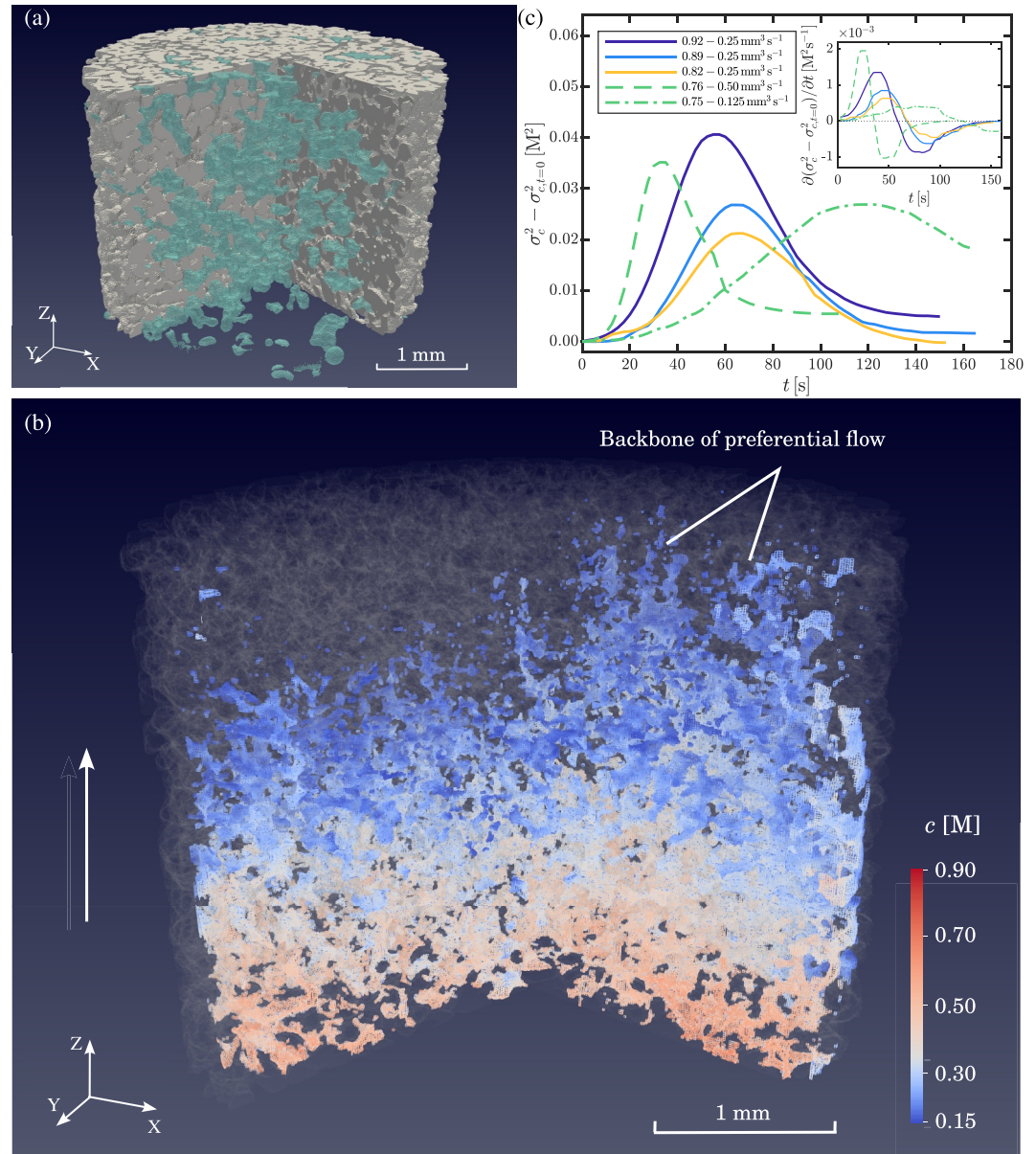
Figure 1. Concentration field and mixing quantification from synchrotron X-ray micro-tomography experiments. (a) 3D reconstruction of the tested porous medium. Only three-quarters of the sample are displayed to allow the visualization of the gas phase (air, shown in cyan) inside of the pore space for the experiment performed at $S_w = 0.82$. (b) Concentration field expressed in units of mole per unit of volume (molar concentration, M) for the transport experiment performed at $S_w = 0.82$ with a flow rate $q = 0.25$ mm^3 s^{-1} at time $t = 50.4$ s after the tracer entered the sample. Refer to Movie S1 in the Supporting Information for a visualization of the entire time series. All concentration values lower than 0.15 M are not displayed for improved visualization. For the same purpose, the air phase is also not shown, whereas the solid phase of borosilicate glass grains is shown as gray transparency. Only three-quarters of the sample are displayed to better visualize the concentration differences inside the pore space. The white arrow indicates the main flow direction. The formation of a backbone of preferential flow, that is, preferential flow channels, is indicated on the upper right portion of the sample. (c) Evolution of the variance of the concentration field, σ_c^2, in time for all five transport experiments. The values of σ_c^2 have been corrected by the variance at time $t = 0$ s, $\sigma_{c,t=0}^2$. Different line types correspond to different injection flow rates, whereas different line colors correspond to different saturation degrees. Note that, in that regard and for facilitating experiment comparison, we have grouped together $S_w = 0.76$ and $S_w = 0.75$ given their very similar saturation degree. The inset shows the rate of change of σ_c^2 over time, $\partial(\sigma_c^2 - \sigma_{c,t=0}^2)/\partial t$, for every experiment.

Table 1
Summary of the Flow Characterization for All Experiments Reported in This Study, and Additionally Also for the Case $S_w = 1.00$, *Which Was Built Up From the Combination of the Segmented Tomograms of the Liquid (KI Solution) and the Gas (Air) Phase*

S_w [−]	q [mm³ s⁻¹]	$\bar{v}$ [×10⁻⁴ m s⁻¹]	Pe [−]	Ca [×10⁻⁶]	PV [−]
1.00	0.250	1.49	2.32	1.78	−
0.92	0.250	1.85	2.88	2.21	5.13
0.89	0.250	1.49	2.31	1.77	5.00
0.82	0.250	1.96	3.05	2.34	5.44
0.76	0.500	4.68	7.28	5.58	7.84
0.75	0.125	1.09	1.69	1.30	3.33

Note. Values reported here were computed from the numerical flow simulations. Flow descriptors include the injection flow rate, q, the mean fluid flow velocity, $\bar{v}$, the Péclet number, Pe, the capillary number, Ca, and the total number of injected pore volumes during the entire experiment, PV. For the computation of both Pe and Ca, we used the average properties of the KI solution over the range of concentrations chosen for the experiments (0.06–0.90 M) and at a temperature of 25°C.

solution in the range of concentrations used in the experiment at a temperature of 25°C, respectively. Table 1 summarizes the single C_a and $\bar{v}$ values obtained for every experiment.

Very high spatial and temporal resolutions, unprecedented for transport studies in porous media, were essential for the purpose of this study, given the rapid nature of the observed processes. Each tomographic data set consisted of $2016 \times 2016 \times 1100$ isotropic voxels of lateral size of 2.75 μm, acquired over a total time of 2.4 s (approximately 15% smaller voxel size and 60% faster acquisition time compared to similar studies (Hasan et al., 2020)). This included the time required for the acceleration, rotation (from 0° up to 180° around the cylindrical sample symmetry, vertical axis), and deceleration of the sample (1.2 s in total), during which a total of 500 angular projections, that is, radiographs, of the sample were collected. In particular, the total tomographic acquisition time needed to be smaller than the time scales of the solute's advection and diffusion over the average pore size. The remaining 1.2 s were needed for rotating the sample back to a position of 0°. This was required since the inlet and outlet lines were connected without a slip ring, hence not allowing for an uninterrupted rotation of the sample. To avoid motion artifacts in the reconstruction, we made sure that the sample's movement during rotation with respect to the vertical axis was kept smaller than the voxel size. In addition, the acceleration and deceleration of the sample back and forth movement together with the achieved low capillary numbers, led to non-rotating flow conditions. The tomographic image acquisition was achieved by using almost monochromatic radiation at an energy of 21 keV, to be able to capture concentration gradients and to estimate quantitatively concentration values inside the pore space. Each experiment's set of results included a total of 250 tomograms, that is, 250 time steps, for a total of eight experiments. This work focuses on the results from five of them. Before starting each experiment, we acquired 10 radiographs in the absence of the X-ray beam (so-called dark-current radiographs) and 100 of them in the presence of the beam but with the sample out of the beam (so-called flat-field radiographs). Both sets of radiographs were then used for the usual dark-current and flat-field corrections of the sample's radiographs, at any successive point in the time series. We used as X-ray detector the system available at the TOMCAT beamline, consisting of (a) a 150 μm-thick LuAg:Ce scintillator screen, converting the X-ray photons into visible light ones; (b) a high-efficiency visible light microscope, called macroscope (Bührer et al., 2019), which, in our case, was set to provide a 4× geometrical magnification; and (c) the high throughput GigaFRoST detection and read-out system (Marone et al., 2020), including a sCMOS chip as visible light photons detector (PCO.Dimax by PCO GmbH, with 11 μm physical pixel size). The detector's exposure time for acquiring each radiograph was 2 ms.

The tomograms were reconstructed using the beamline's software and hardware infrastructure, relying upon TOMCAT in-house-developed Fourier space re-gridding algorithm (Marone & Stampanoni, 2012). In correspondence with each point in the tomographic time series, we reconstructed two types of tomograms. The first one assumed only X-ray absorption as the main image formation mechanism (contrast mechanism), using the Beer-Lambert law for relating radiographic pixel values to the linear projection of the X-ray linear attenuation coefficient along the respective ray hitting the detector at such pixel (Als-Nielsen & McMorrow, 2011). The second type of reconstruction assumed X-ray refraction as the main contrast source (so-called phase-contrast tomogram). In this case, the phase retrieval, that is, the calculation of the linear projection of the real part of the X-ray index of refraction from the radiographic pixel value, was performed with an implementation of the algorithm proposed by Paganin et al. (2002), with an estimated ratio of real-to-imaginary parts of the complex-valued X-ray index of refraction, δ/β, of about 371. We note that at each time point during every experiment, our acquired tomographic data sets contained both X-ray absorption and refraction information. This was achieved by the sample being located at a distance from the detector, d_{S-D}, equal to 20 mm, which laid within the Fresnel diffraction region of the imaging configuration. Such downstream region past the object is where refraction effects on the X-ray beam propagation can be still exploited for the phase retrieval type based upon the cited approach by Paganin et al. (2002). At the mentioned X-ray photon energy of 21 keV, the Fresnel number, N_F, of the imaging configuration could be estimated as $N_F = l_d^2/(\lambda\,d_{S-D}) \approx 25.6$, where λ is the X-ray wavelength (in vacuum)

corresponding to 21 keV and l_d is the adopted level of detail of the sample. This was chosen equal to an upper bound of the effective, tomographic spatial resolution, being equal to twice the voxel size, $l_d = 5.5$ μm. By its definition, within the Fresnel diffraction region of the imaging configuration $N_F \geq 1$. The cited phase retrieval approach by Paganin et al. (2002) requires $N_F \gg 1$, a condition well satisfied in our case. Images of the experimental setup and of the sample are shown in Figure S2 in Supporting Information S1. As expanded in Section 2.2, the experiments post-processing relied primarily on the phase-contrast tomograms.

2.2. Experimental Concentration Calibration

In addition to the high spatial and temporal resolutions, X-ray micro-tomography with almost monochromatic and highly spatially coherent synchrotron radiation allowed us to achieve a statistically robust mapping of image voxel values to actual solute concentration ones (expressed in molar, M). The experimental calibration of the tomograms' voxel values versus the solute's concentration values was achieved via a set of fourteen, single tomogram experiments. They involved the sample fully saturated with an aqueous KI solution at different concentration values, in the range from 0.06 to 1.81 M. The obtained calibration curve, created following the procedure presented in Lavin et al. (2018) and in Bevington and Robinson (2003), describes a linear relationship between the directly measured voxel value and the corresponding solution concentration inside the liquid phase. It also describes a rather narrow confidence band (see Figure S3 in Supporting Information S1). The calibration curve was obtained by employing the 32-bit phase-contrast tomograms, considering only the regions occupied by the liquid phase, as obtained from segmentation (see Section 2.3). We chose the phase-contrast tomograms because they showed a smaller coefficient of variation of the voxel values in comparison with the absorption tomograms, that is, a smaller ratio between the standard deviation computed from all voxels inside the liquid phase relative to their mean value. In general, we observed a slight heteroscedastic behavior of such voxel values across concentrations, with a slight increase in standard deviation toward the lower range of concentrations. Not much difference was observed between 32-bit and 16-bit tomograms, the latter obtained from the former by a coarser quantization of a 32-bit voxel value range chosen identical at any concentration, that is, an identical dynamic range. However, we decided to use the 32-bit tomograms for the calibration and also for further analysis of the transport experiments since they are not affected by the dynamic range chosen for the image reconstruction. Hence, we could guarantee no bias in the calibration curve derivation as well as in any successive steps of the image analysis protocol described below. In addition to the linear mapping accuracy, the temporal stability of all components of the TOMCAT tomography beamline allowed for achieving high temporal consistency in such mapping. All these features further highlight the capabilities and advantages offered by this experimental technique in studying transport processes at the pore scale. Further details on the mathematical derivation of the calibration curve and on the corresponding uncertainty analysis are presented in the Supporting Information S1, Text S1.

2.3. Image Analysis

We defined an image analysis protocol for the post-processing of the transport experiment tomograms. Out of the 250 of them available per experiment, we applied such protocol to a total of 44 for the experiment performed at $q = 0.50$ mm^3 s^{-1} and on an average of 65 of them for the remaining cases. We did not use, in any experiment, all 250 tomograms since the arrival, spreading, and mixing of the solute occurred only during specific time intervals shorter than the overall experiment duration. The latter was chosen long enough to be sure of always including enough duration to fully observe, and thus analyze, those processes. This is indicated in Table 1, which summarizes the total number of pore volumes, PV, that is, the ratio of injected volume relative to the total volume of the liquid phase, injected over the chosen range of scans for every experiment. We first applied a 2D (XY planes, orthogonal to the cylindrical specimen's symmetry axis) non-local means denoising algorithm (Buades et al., 2005), implemented in the software Avizo (ThermoFisher Scientific, 2022), on the full 32-bit tomographic slice stack of each one of those tomograms. No significant improvement was observed when applying the same algorithm in 3D. We then employed the Active Contours plugin available in the open source software Icy (version 2.1.3.0) (De Chaumont et al., 2012a, 2012b) to generate a binary tomogram acting as a sample mask, that is, to segment the sample's volume only. The latter is an 8-bit tomogram with only two possible voxel values: either 255, to indicate that a voxel is located inside the sample's volume, or 0, to indicate the opposite. Such sample mask allowed excluding the imaged areas surrounding the cylindrical sample from further analysis. Only one sample mask was generated per experiment. The remaining steps in the image analysis protocol were performed using the open-source software ImageJ (Schneider et al., 2012a, 2012b), in particular, the Xlib plugin library

(Münch, 2022). We aimed at creating accurate phase material masks (i.e., binary 8-bit tomograms of the liquid, gas, and solid phases, respectively) of every analyzed tomogram, for extraction of single-phase image information. In the first step, we applied a K-means clustering algorithm (Lloyd, 1982) on the 16-bit tomograms at each time instant. This aimed at associating all voxels belonging to every material phase to one single, distinct image voxel value. This was followed by a segmentation protocol, which also combined artifacts removal (3D fill holes morphological operator) and background removal algorithms, resulting in corrected, binary masks for every material phase of the analyzed tomogram. The liquid phase binary mask was then used on the denoised version of the original 32-bit tomograms for extracting a final tomogram containing experimental information only in voxels belonging to this phase. This was performed in the same fashion for the air phase. The post-processing and analysis of the transport experiments were carried out using these final tomograms. A graphical summary of the image analysis protocol is shown in Figure S4 of the Supporting Information S1.

2.4. Solute Advance Front Reconstruction

Our analysis of the mechanisms controlling the mixing behavior observed in the experimental results required the reconstruction of the solute plume's front. This was represented via the isosurface of 50% concentration ($c = 0.48$ M for the range of concentrations used in this study). To reconstruct this isosurface, we first used the software Paraview (Kitware, 2023) to threshold the denoised 32-bit liquid phase tomograms and to extract single voxels belonging to the 49.8%–50.2% concentration range. We created an analysis pipeline, implemented in Matlab (The MathWorks, 2022), first to interpolate the obtained point cloud and to generate a continuous surface. We then corrected this surface using the liquid phase mask (see Section 2.3) to overwrite and set as image background all positions belonging to either the solid or the gas phase. The corresponding surface area was obtained by first triangulating the corrected isosurface using a moving observation window at the voxel scale of the images and then adding up the surface area of single triangular planes. Triangulation also allowed the generation of single *.stl files for reconstructing the corrected isosurface.

2.5. Numerical Simulations of Flow

Given the impossibility of obtaining a fully resolved velocity field from the experimental data only, we complemented our data set with additional 3D numerical simulations of flow. They consist in the solution of the Stokes flow equation for non-compressible flow for all experimental cases and also for the additional case $S_w = 1.00$. In these simulations, the spatial domain corresponded with the one occupied by the resident solution, thus the space throughout which transport and mixing occurred. Such spatial domain was obtained from a tomogram corresponding to a time step chosen at about half of each experiment duration, via the image analysis workflow presented in Supporting Information S1 (see Figure S4 for a schematic summary of such workflow). Such digitized spatial domain was downsampled by a factor of five, compared with the original voxel size, thus leading to a spatial discretization scale of 13.75 μm. We also added the case $S_w = 1.00$ by using the tomogram of the entire sample's pore space. The tetrahedral meshing of the segmented liquid phase region was performed using the fTetWild algorithm (Hu et al., 2020) on these full-sample liquid phase masks. The obtained meshes were then imported into the Finite Elements Method software COMSOL Multiphysics for further analysis. Different boundary conditions were applied to simulate the same conditions tested during the experiments. They included a fixed inflow velocity at the inlet cross-section, a constant pressure at the outlet, and a no-slip boundary condition (zero velocity at the boundary) at all material interfaces. The use of the latter at the interface liquid-gas has been demonstrated to have a negligible impact, both in 2D and in 3D, on fluid flow velocity distributions in porous media (Guédon et al., 2019; Triadis et al., 2019). Further details on the numerical model setup can be found in the Supporting Information S1, Text S2. The main outputs of the simulations included resultant velocity magnitude and velocity tensor, vorticity tensor, shear rate tensor, and pressure at every node location. The values of such fields were extracted at a four-times smaller spatial resolution than that of the experimental data sets, that is, over a regular grid of size 11 μm in all three principal directions. The results' post-processing revealed that PDFs of the listed fields' values experienced no significant variations when the numerical results were extracted at higher spatial resolutions. In the same fashion, no significant variations in the PDFs scalings were observed when using higher-resolution liquid phase masks for mesh generation. Both the resultant velocity fields and the vorticity magnitude fields obtained for every performed simulation are shown in Figures S5 and S6 of the Supporting Information S1, respectively.

3. Theoretical Concepts and Metrics

3.1. Variance of the Concentration Field

The experimental concentration calibration allowed representing the tomographic data sets obtained from the synchrotron X-ray micro-tomography experiments as fields of solute concentration $c(\mathbf{x}, t)$ for every time step at every location of the pore space occupied by the liquid phase. We quantify mixing from these data sets in terms of concentration statistics, in particular through computation of the variance of the concentration field $\sigma_c^2(t)$ at every time step t (Dentz et al., 2022; Jha et al., 2011). $\sigma_c^2(t)$ can be expressed as

$$\sigma_c^2(t) = \langle c(\mathbf{x}, t)^2 \rangle - \langle c(\mathbf{x}, t) \rangle^2, \tag{1}$$

where $\langle \cdot \rangle$ denotes the expected value over the entire ensemble of voxels in the liquid phase. σ_c^2 is thus a measure of the heterogeneity of the mixture, providing a good proxy for the amount of segregation existing between the resident solution and the continuously injected solute during the entire experiment duration.

3.2. Euler Characteristic

Recent studies have highlighted the role of the topological complexity inherent to porous media in driving local fluid stretching, ultimately controlling transport, mixing, reactions, and biological processes occurring in porous systems (Lester et al., 2013, 2016). In order to assess this aspect, we first rely on a geometrical characterization of the wetting liquid phase topology, by means of the Euler characteristic χ, a topological invariant widely used in soil and porous systems research (Armstrong et al., 2019; Lester et al., 2016; Schlüter et al., 2016; Shih et al., 2022). In particular, it can be used to characterize the connectivity of the porous system, with strong implications on the divergence or convergence of streamlines, as it is directly linked to the dynamics of the skin friction field, that is, to the occurrence of separation and reattachment points along boundary surfaces (Lester et al., 2016). It can be defined based on entities that describe a spatial region (Vogel, 2002) (the pore space in this case) as

$$\chi = N - C + H, \tag{2}$$

where N is the number of isolated objects or clusters in the analyzed spatial domain, C is the number of redundant connections or loops, and H is the number of completely enclosed cavities. Negative values of χ describe a well-connected system, as it is usually the case for porous media, given that generally $N < C$ (Lester et al., 2016). Equation 2 can be expressed alternatively as a function of the number of voxels (n_c), faces (n_f), edges (n_e), and vertices (n_v) that form the 3D binary image representing the target geometrical domain (Michielsen & De Raedt, 2001), which in our case corresponds to the liquid wetting phase of every experiment. This results in

$$\chi = -n_c + n_f - n_e + n_v. \tag{3}$$

We used an optimized algorithm based on the immediate vicinity of every single voxel in the 3D binary tomogram of the segmented liquid phase, together with binary decision diagrams (Blasquez & Poiraudeau, 2003) for the computation of χ according to Equation 3.

3.3. Helicity Density

To further explore the impact of the liquid phase topology on flow streamlines, we also study the formation of secondary flows. In particular, we focus on the occurrence of helicity, a kinematical property that provides a quantitative measure of the spatial complexity of flow fields and that remains constant despite fluid deformation (Moffatt, 1992; Sposito, 2001). We quantify it through the helicity density h, which is expressed as the scalar product of the velocity vector $\left(\overrightarrow{v}\right)$ and the vorticity vector $\left(\overrightarrow{\omega}\right)$ fields

$$h = \overrightarrow{v} \cdot \overrightarrow{\omega}. \tag{4}$$

Both the velocity and vorticity fields were obtained from the numerical simulations of flow. The spatial distribution of both the resultant velocity magnitude and the vorticity magnitude over the entire pore space for all experiments are presented in Figures S5 and S6 of the Supporting Information S1, respectively.

3.4. Q-Criterion

To further investigate the mechanisms controlling mixing in unsaturated porous media, we studied the control that the liquid phase saturation exerts on the interplay between the flow's shear deformation and the rotational one. The former results from local velocity differences along neighboring streamlines, whereas the latter is induced by the occurrence of helical flow. For such purpose, we computed the Q-criterion (Hunt et al., 1988), an index that allows for vortex identification, suitable for the case of steady non-rotational flows (Haller, 2005). It is expressed using the invariants of the 3D velocity gradient tensor, $\nabla \vec{v}$, that is, the deformation rate tensor. It identifies a vortex whenever the second invariant, Q, of $\nabla \vec{v}$ is larger than zero, that is

$$Q = \frac{1}{2} \left(\|\mathbf{\Omega}\|^2 - \|\mathbf{S}\|^2 \right) > 0, \tag{5}$$

where $\|\cdot\|$ indicates the Frobenius norm, $\mathbf{\Omega}$ is the non-symmetric portion of $\nabla \vec{v}$, that is, the vorticity tensor, and $\mathbf{S}$ is the symmetric counterpart of $\nabla \vec{v}$, that is, the shear strain rate tensor (Hunt et al., 1988). Therefore, it can be used to locally quantify the excess of the rotation strain rate relative to the shear strain rate, hence hinting at the main mechanism behind local solute plume deformation. In addition, the Q-criterion also requires the pressure to be minimal compared to the ambient pressure inside the region identified as a vortex, as this guarantees that the neighboring streamlines are indeed curved (Hunt et al., 1988).

4. Results and Discussion

4.1. Lower Saturation Enhances Mixing Via a Stronger Solute Front Deformation

Results from five experiments are reported in this work, which cover saturation degrees spanning from 0.75 to 0.92 and tracer injection flow rates (q) ranging from 0.125 mm^3 s^{-1} to 0.50 mm^3 s^{-1}. The latter values correspond to Péclet numbers, Pe, ranging from $Pe = 1.69$ to $Pe = 7.28$, respectively, where Pe represents the ratio between the characteristic time of diffusion and the characteristic time of advection over a typical pore size. It can be expressed as $Pe = \bar{v}\bar{\xi}/2D$, where $\bar{v}$ is the mean flow velocity of every experiment, $D = 1.929 \times 10^{-9}$ m^2 s^{-1} is the average diffusion coefficient of the KI solution in the range of concentrations used in the experiment (Dunlop & Stokes, 1951), and $\bar{\xi} = 30$ µm is the average pore size, computed from the distribution of pore sizes as shown in the Figure S1 in Supporting Information S1. Table 1 summarizes the Pe numbers obtained for every experiment. Figure 1b depicts the reconstructed concentration field for an experiment performed at $S_w = 0.82$ and at $q = 0.25$ mm^3 s^{-1} at time $t = 50.4$ s after the tracer entered the sample, that is, around 1/3 of the total experiment duration (refer to Movie S1 in the Supporting Information for the entire time series). The combined effect of the porous medium heterogeneity and the presence of an immiscible-immobile phase manifests itself in the formation of preferential pathways, as highlighted in Figure 1b, which are usually referred to as the backbone of preferential flow (De Gennes, 1983). This flow structure consists of channels of high velocity that allow for faster displacement of the tracer and for most of its transport.

We relied on the variance of the concentration field σ_c^2 (Dentz et al., 2022; Jha et al., 2011) to quantify and compare the mixing behavior across experiments. Figure 1c shows the variation in $\sigma_c^2 - \sigma_{c,t=0}^2$ over time, for all experiments, where $\sigma_{c,t=0}^2$ is the variance of the concentration field at time $t = 0$ s. This subtraction was applied to correct for some remaining noise in the tomograms at lower concentration values, right before starting the transport experiments, causing σ_c^2 at $t = 0$ s to slightly deviate from zero, that is, when the entire porous space is occupied by the resident solution only. The results show an overall enhancement of mixing at lower S_w. All cases exhibit two clear phases. In the first phase at early times, both advection and diffusion contribute to solute transport, with the former controlling the increasing segregation of the two mixing liquids as the tracer enters the sample. This is reflected in an increase of σ_c^2 over time. Note here that the plume does not enter as a sharp front, since already some diffusion occurred at the inlet. A second phase begins at the stage of maximum segregation, that is, highest $\sigma_c^2 - \sigma_{c,t=0}^2$, promoting the mixing of both tracer and resident solution. This reflects itself in a
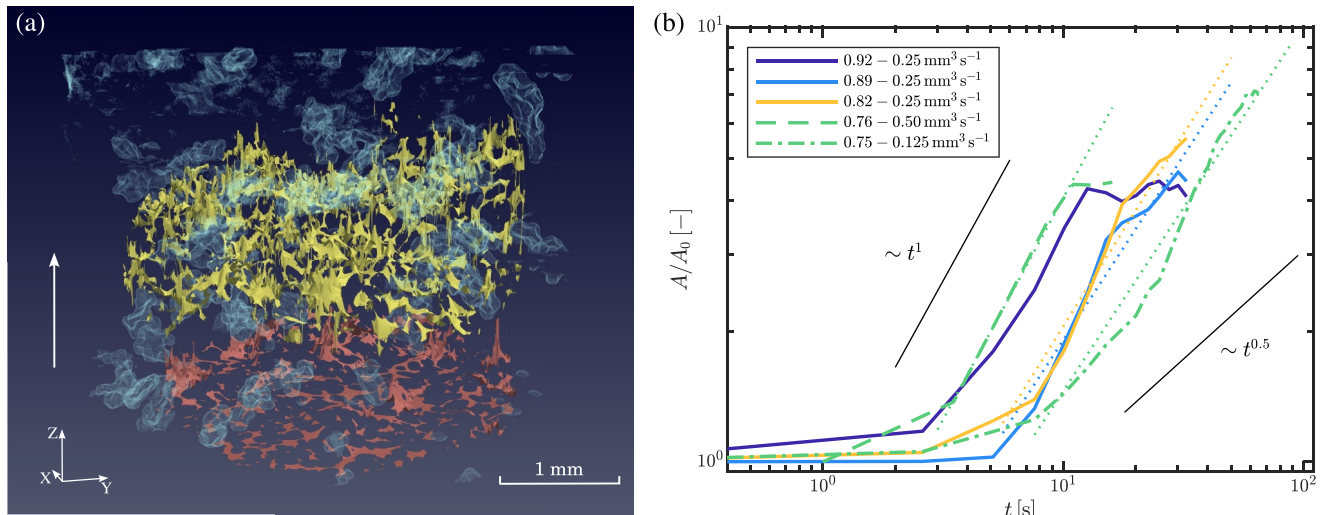
Figure 2. Analysis of the solute front deformation over time, as a function of the saturation degree. (a) Deformation over time of the plume's advancing front, here represented by the isosurface of 50% of concentration, shown at the time instants $t = 30$ s (in light red) and $t = 60$ s (in yellow), for the experiment performed at $S_w = 0.92$ and flow rate $q = 0.25$ mm^3 s^{-1} (refer to Movie S2 in the Supporting Information for a visualization of the entire time series). The solid phase of borosilicate glass grains is not displayed to improve the visualization, while the gas phase (air) is shown in semi-transparent cyan. The white arrow indicates the main flow direction. (b) Temporal evolution of the area of the advancing front, A, normalized by the area computed at the initial time of the deformation analysis, A_0. Different line types correspond to different injection flow rates, whereas different line colors correspond to different saturation degrees. Note that, in that regard and for facilitating experiment comparison, we have grouped together $S_w = 0.76$ and $S_w = 0.75$ given their very similar saturation degree. The respective power law fitting curves are displayed with dot lines for all cases except for $S_w = 0.92$, which is the only case that reaches a plateau at later times. Scalings for both a ballistic ($A/A_0 \sim t^1$) and a Fickian ($A/A_0 \sim t^{0.5}$) regime are displayed for visual reference.

decreasing σ_c^2 in time. Results show that for the same q, lower S_w leads to smaller σ_c^2, hence it induces a faster smoothing of the concentration gradients formed in the pore space during the transport process. At very similar S_w (less than 1% difference, i.e., cases $S_w = 0.76$ and $S_w = 0.75$), a higher q reduces the transit time of the solute, allowing for a more segregated condition to build up in the pore volume. This reflects itself in higher σ_c^2 values at early times, after which σ_c^2 rapidly decreases toward a well-mixed condition. Reducing q allows for diffusion to more effectively smooth out concentration gradients in the system before the plume has been largely dispersed. The latter point is better depicted when plotting $\sigma_c^2 - \sigma_{c,t=0}^2$ against the dimensionless time $\tau = t/t_{\text{adv}}$, where the advective time, $t_{\text{adv}} = \bar{\xi}/\bar{v}$, is the time required for the flow to bridge the average pore size $\bar{\xi}$ at the average flow velocity $\bar{v}$. This is shown in Figure S7 in Supporting Information S1, in which, after an identical increase of $\sigma_c^2 - \sigma_{c,t=0}^2$ in time for both $S_w = 0.76$ and $S_w = 0.75$, the latter case describes a lower maximum σ_c^2.

The mixing analysis described so far can be further explained by taking a look at the derivative in time of the variance of concentration, $\partial(\sigma_c^2 - \sigma_{c,t=0}^2)/\partial t$, that is, to the rate of change of segregation in time, as shown in the inset on Figure 1c. Under the same q, lower S_w described the lowest absolute $\partial \sigma_c^2/\partial t$ values among all cases tested experimentally, both in the phase of initial segregation and in the following diffusion dominated phase. The former can be explained by concentration gradients being enhanced in the liquid phase at lower S_w (Jiménez-Martínez et al., 2015; Markale et al., 2021) already at early times, resulting in a larger diffusive flux countering the segregation effect induced by advection. The latter is associated to incomplete mixing, that is, the formation of not-fully mixed regions behind the plume's front, in which transport is mainly driven by diffusion, and whose formation is enhanced as saturation decreases (Markale et al., 2021).

The mechanism behind this mixing behavior is explained by looking at the evolution in time of the interface between the injected and the resident solution, that is, at the plume's front where diffusion takes place. This interface between both mixing solutions can be analogously represented by the isosurface of 50% concentration ($c = 0.48$ M for the range of concentrations used in this study). Figure 2a shows such surface for $S_w = 0.92$ and $q = 0.25$ mm^3 s^{-1} at two specific time steps, $t = 30$ s shown in light red and $t = 60$ s shown in yellow (see Movie S2 in the Supporting Information for the entire time series). The latter depicts an increase in the isosurface deformation as it moves through the sample, compared with an initial condition depicted by the former, when
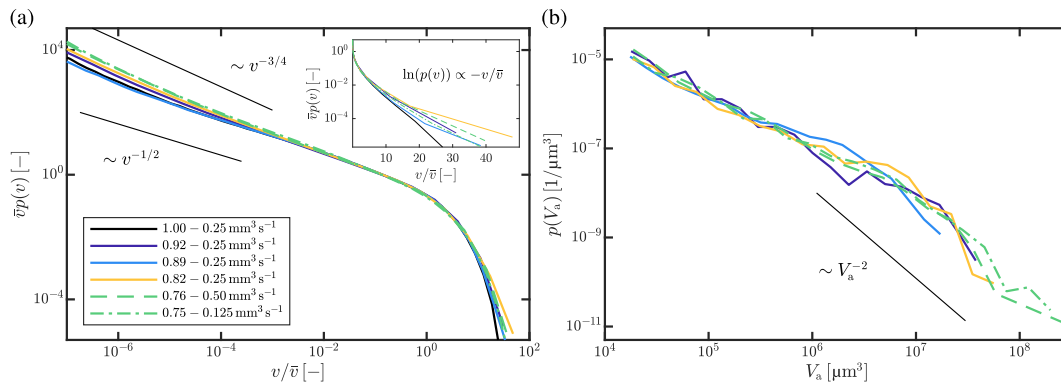
Figure 3. Hydrodynamic characterization and air clusters volume distribution as a function of saturation degree. (a) Probability density function (PDF) of the liquid flow velocity magnitude, $p(v)$, computed in each case via 3D flow Finite Elements Method (FEM)-based numerical simulations. $p(v)$ has been normalized by the corresponding average velocity magnitude value, $\bar{v}$. $p(v)$ for the additional case $S_w = 1.00$ is also included. The Log-Log scale highlights the scaling of the low-velocity magnitudes, with exact power-law scalings also shown for visual reference only. A semi-Log plot is shown in the inset to display the exponential behavior at high-velocity magnitudes. (b) PDF of the volume of air clusters, $p(V_a)$, for all experiments. $p(V_a)$ is expressed in units of μm^3. The minimum volume considered corresponds to that of an average pore of size $\bar{\xi} = 30$ μm. The power-law scaling V_a^{-2} is shown for visual reference. In both panels, different line types correspond to different injection flow rates, whereas different line colors correspond to different saturation degrees. Note that, in that regard, we have grouped together $S_w = 0.76$ and $S_w = 0.75$ given their very similar saturation degree.

almost no deformation is visible. This feature is analyzed quantitatively in Figure 2b, which shows, for all experiments, the increase in time of the area, A, of the isosurface over the sample's imaged length. For comparison, A has been divided by the corresponding value at the first time step considered in the analysis, A_0. Note the shorter time range used for this analysis compared to the entire duration of the experiment, as reported in Figure 1c. That is because only time instants, at which the entire 50% concentration isosurface can be found inside the sample, are considered. Figure 2b shows that at high $S_w = 0.92$, the system still remains fairly homogeneous, causing a piston-like movement of the isosurface after some initial deformation has occurred, as indicated by the plateau reached at long times (after $t \sim 11$ s) (Jiménez-Martínez et al., 2015). For lower S_w and under a constant q, we observed an enhancement of the isosurface deformation over time, manifested both in a larger maximum relative deformation and in a larger power-regression exponent (refer to Table S1 in Supporting Information S1, for the magnitude of these exponents). The larger the volume of air in the pore space, the more the number of obstacles to be bypassed by the solute's plume to move through the system, enhancing the plume's dispersion and stretching. At very similar S_w, an increase of q leads to a higher rate of deformation in time. We hypothesize that the isosurface deformation will eventually reach a plateau at late times for all cases, given both the effect of diffusion recovering some of the deformation that occurred as the plume moves through the system and the finite size of the tested domain. In summary, both lower S_w and higher q enhance front deformation, increasing at a higher rate the interface area where mixing between the resident and the injected solution occurs. This translates into increased diffusive flux and enhanced mixing efficiency, that is, smaller σ_c^2 (Jiménez-Martínez et al., 2015, 2017). The results here reported show a super-diffusive scaling of A with time, in all cases, which highlights the non-Fickian nature of transport in unsaturated porous media (Jiménez-Martínez et al., 2017; Velásquez-Parra et al., 2022). Detailed information on the estimation and magnitude of the power-regression scalings shown in Figure 2b can be found in the Supporting Information S1, Text S3.

4.2. Dependence of Mixing on Hydrodynamics and Air Clusters Volume

The different mixing regimes as a function of S_w can be further described by looking at the liquid flow velocities in the pore space. Figure 3a shows the probability density function (PDF), $p(v)$, obtained for the liquid flow velocity magnitude, v, as estimated for all cases from numerical simulations of flow. Further details on the numerical simulations are presented in the Materials and Methods section and in the Supporting Information S1, Text S2, where also a full visualization of the scalar field v is presented (see Figure S5 in Supporting Information S1). The velocity magnitude PDFs are characterized by two regimes, a power law-like behavior for low-velocity magnitudes, and an exponential scaling for high v-values, in agreement with both experimental and numerical results already reported in the literature (Datta et al., 2013; Guédon et al., 2019; Souzy et al., 2020; Velásquez-Parra et al., 2022). Note here the power law behavior obtained for the low-velocity range under fully
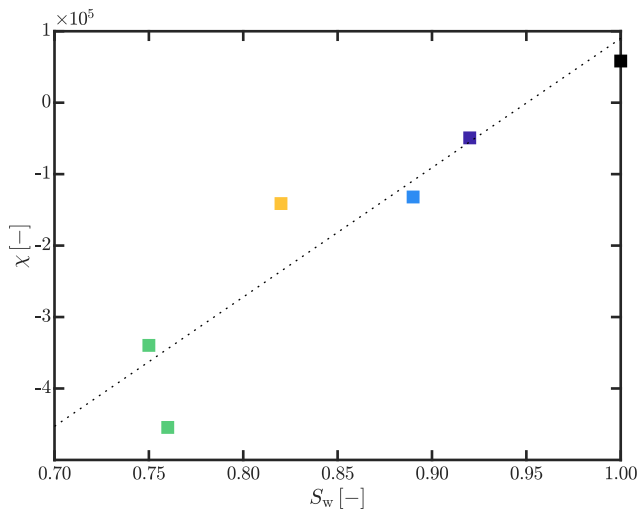
Figure 4. Euler characteristic, χ, of the liquid phase, as a function of saturation degree S_w, computed for every experiment at a single time step chosen at about half of its duration. Results were obtained in each case from binary tomographic images of the liquid phase of the entire sample (liquid phase mask, see Figure S4 in the Supporting Information S1). A fully saturated condition $S_w = 1.00$ is also displayed for comparison. The best fitting line is displayed black dotted. The color criteria used for the markers follows the same one used in Figures 1c and 2b.

saturated conditions, which reflects the role of the solid phase heterogeneity in leading to velocity magnitude PDFs that differ from those obtained in the presence of Poiseuille velocity distributions, as it is often the case in 2D analyses performed under idealized conditions (de Anna et al., 2017). Lower S_w leads to a broader $p(v)$, characterized both by larger maximum velocities under constant q and by a larger $p(v)$-value at lower velocity magnitudes. This reflects an enhancement of the so-called backbone, where large velocities are reached and through which most of the solute is transported, and of the so-called dead-ends of low velocities, which are less accessible for the solute (De Gennes, 1983; Velásquez-Parra et al., 2022). Transport in these dead-ends is strongly influenced by molecular diffusion, as it is the main control on the solute's long residence times experienced in the presence of such low flow velocities. The enhancement of these two flow structures (backbone and dead-ends) translates into larger concentration gradients at their interface, in correspondence of lower S_w (Jiménez-Martínez et al., 2015), increasing the diffusive flux between them and further explaining the mixing enhancement.

Single differences in the trend described so far for $p(v)$ as a function of S_w are obtained for $S_w = 0.89$, which displays a less negative power law scaling for low velocities than $S_w = 0.92$. This difference is explained by the volume of air clusters inside the pore space, whose PDF $p(V_a)$ is shown in Figure 3b. Only volumes equal to or larger than the volume of an average pore, assumed equal to that of a sphere with a diameter equal to the estimated average pore size $\bar{\xi} = 30$ μm, were considered, since they represent the gas phase hosted in the system by capillary forces. We observe a change in the $p(V_a)$ scaling at an air cluster volume $V_a \sim 1 \times 10^6$ μm³, after which $p(V_a)$ shows for all cases a power law distribution with a scaling $p(V_a) \sim V_a^{-2}$ that very well matches previously published results obtained for 2D conditions (Jiménez-Martínez et al., 2017; Tallakstad, Løvoll, et al., 2009). This volume corresponds to that of a cluster with a size of approximately three average pore sizes. Counter-intuitively, Figure 3b depicts a narrower distribution for $S_w = 0.89$ than for $S_w = 0.92$, which translates into smaller air clusters in spite of the overall larger relative volume of air inside the pore space. This denotes a weaker effect of the air clusters at blocking the flow, leading to less enhancement of preferential pathways and dead-ends than for $S_w = 0.92$, as observed in its $p(v)$. For the remaining cases, a reduction of S_w leads to larger air cluster volumes as expected. These results point out the non-uniqueness of these multiphase systems and highlight the importance of both the air cluster volumes and their spatial distribution for defining the system's heterogeneity. These two elements further explain differences in the final area A of the 50%-concentration isosurface achieved under similar saturation degrees ($S_w \sim 0.75$; Figure 2b).

4.3. Backbone Formation Promotes Helicity

To explain the mechanisms behind the isosurface deformation reconstructed from the experiments and presented in Figure 2a, we first characterize the liquid phase connectivity using as an index the Euler characteristic χ (see Equation 2). Figure 4 shows a linear decrease of χ with decreasing S_w for the range of S_w considered in this work. Lower S_w thus improves the system's capacity for joining initially separated entities, due mainly to the formation of new redundant loops, that is, larger C in Equation 2. This promotes the spatial convergence of flow streamlines, increasing their tortuosity, as they now follow these newly opened loops and can connect to other distant pathways. Consequently, the formation of the preferential flow backbone is enhanced, as also shown by the increase of high velocities in the inset of Figure 3a. Similar variations of χ as a function of S_w have been observed for the connectivity of the non-wetting phase (Armstrong et al., 2016; Schlüter et al., 2016; Xu et al., 2020) and also of the wetting phase under imbibition-drainage cycles (Schlüter et al., 2016), although in simplified 3D geometries obtained with packed spherical (instead of irregularly shaped) glass beads. They also suggest an increase of χ at very low saturation degrees (not reached in this study) once non-wetting clusters start isolating portions of the wetting phase (Schlüter et al., 2016), that is, increasing N in Equation 2. Figure 4 also shows significant differences in χ for very similar saturation degrees ($S_w \sim 0.75$), further highlighting the topological non-uniqueness of unsaturated systems in spite of overall similar S_w.
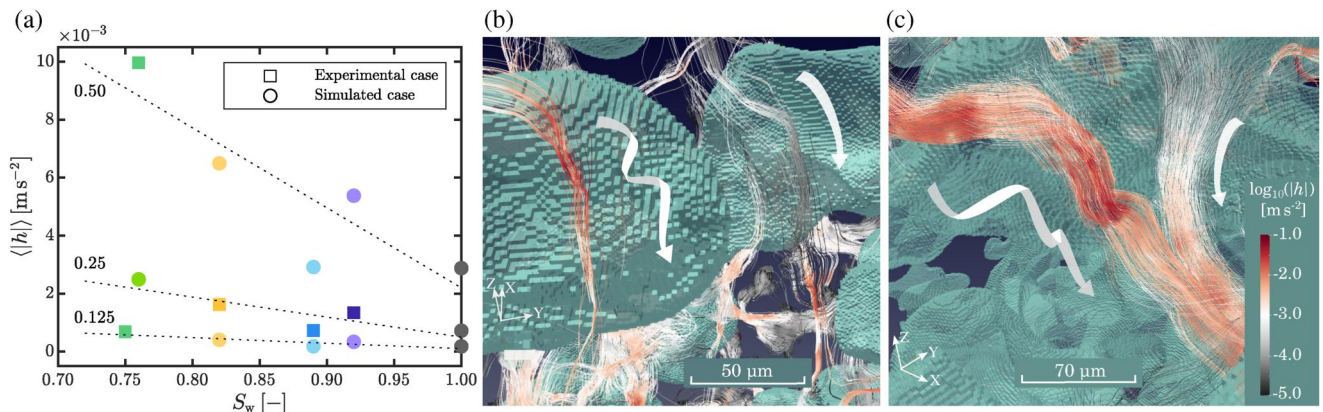
Figure 5. Analysis of the occurrence of helical flow in the pore space. (a) Variation of the average absolute helicity density, $\langle|h|\rangle$, with S_w, for the three experimental injection flow rates $q = 0.125$, 0.25, and 0.50 mm^3 s^{-1}. The conditions investigated experimentally are displayed with squared markers, whereas additional numerically simulated conditions are shown with circular markers. The dotted lines describe the linear trend obtained for the variation of $\langle|h|\rangle$ with S_w. The color criteria corresponds to that of Figures 1c and 2b. (b, c) show different streamlines deformation patterns induced by the occurrence and enhancement of helical flow in the system. These results correspond to the experiment performed at $S_w = 0.75$ and $q = 0.125$ mm^3 s^{-1}, with numerically generated streamlines colored based on the absolute local helicity ($\log_{10}(|h|)$) and with the air phase imaged experimentally displayed in semi-transparent cyan. The borosilicate glass grains are not displayed to improve visibility. White ribbon arrows describe the deformation pattern common to the different groups of streamlines: (b) depicts the braiding of streamlines in the neighborhood of an air bubble (see red streamlines on the left) and the absence of it for streamlines traveling along a backbone (see gray streamlines on the right); (c) depicts the convergence of two groups of streamlines into the same backbone, with one group experiencing strong braiding and folding (red tones) and the other one showcasing no strong streamline deformation (gray tones).

The impact of the liquid phase connectivity changes expressed by χ on the flow streamlines is better understood by analyzing the occurrence of secondary flows, that is, helical flow, which we quantify by computing the helicity density h using Equation 4. The scalar field h is directly related to the topology of the vorticity field itself (Moffatt, 1992), as it reflects the linkage of vortex lines under a given flow field. This is of paramount importance for the analysis of streamlines deformation, as vorticity induces local rotation on streamlines around an axis specified by the direction of $\vec{\omega}$, depending on the local orientation of the velocity field in reference to the vorticity one (Batchelor, 2000; Sposito, 2001). In particular, h has been used in Darcy-scale studies as a topological measure to showcase the occurrence of helical flow under anisotropic hydraulic conductivity fields both in homogeneous and heterogeneous porous media (Chiogna et al., 2014, 2016).

Figure 5a presents the absolute helicity density $\langle|h|\rangle$, averaged over the entire liquid phase, as a function of saturation degree. We have expanded our data set by performing additional numerical simulations to generate the flow field of every experimental saturation degree and also of the case $S_w = 1.00$ for every injection flow rate tested (keeping $C_a < 1.0$). Note that, for this purpose, we have grouped together $S_w = 0.75$ and $S_w = 0.76$ given their very similar magnitude, creating only one additional case for $S_w = 0.76$ at $q = 0.25$ mm^3 s^{-1}. All additional cases are displayed with circular markers, whereas the conditions tested experimentally are displayed with squared markers. Results indicate a linear increase of $\langle|h|\rangle$ as S_w decreases for the range of saturation degrees presented in this work. This indicates that the heterogeneity added to the system by the air clusters enhances the occurrence of helical flow in the liquid phase, which translates into an enhanced role of vortexes in deforming flow streamlines. Figures 5b and 5c depict the case $S_w = 0.75$ and $q = 0.125$ mm^3 s^{-1} as an example, where streamlines have been colored based on the local absolute helicity density and the air phase is shown in cyan. In Figure 5b, the occurrence of strong braiding is visible in the vicinity of an air bubble (see twisted ribbon arrow), which is linked to large $|h|$-values. In contrast, streamlines traveling through the middle section of the nearby flow backbone describe low local $|h|$, showcasing no braiding and low deformation. Similarly, Figure 5c shows the convergence of two backbones into one common pore throat, with one group of streamlines experiencing large braiding and folding while bypassing air clusters, whereas the other group shows no distinctive deformation patterns and low $|h|$. Both cases illustrate the impact of the increased heterogeneity of the system and of the enhanced spatial convergence of streamlines, associated with lower S_w, on streamlines deformation, through mechanisms that have been described as main drivers of enhanced mixing and chaotic mixing behavior (Aref et al., 2017; Thiffeault & Finn, 2006), namely braiding and folding. In particular, the occurrence of braiding has been strongly linked to the existence of non-zero helicity fields (Aref et al., 2017) and reflects characteristics of
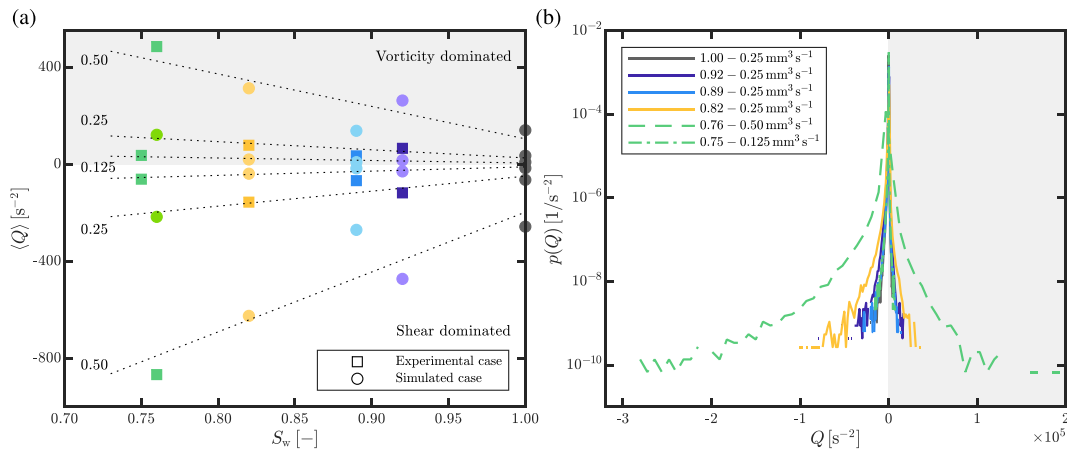
Figure 6. Impact of the saturation degree on how topology controls the solute plume deformation. (a) Average positive and negative Q-criterion, $\langle Q \rangle$, as a function of S_w, for the three experimental injection flow rates, $q = 0.125$, 0.25, and 0.50 mm^3 s^{-1}. The conditions investigated experimentally are displayed with squared markers, whereas additional conditions, created numerically only, are shown with circular markers. The dotted lines describe the linear trends obtained for the variations of the respective indexes as a function of S_w. (b) probability density function of the Q-criterion, $p(Q)$, for the experimental cases only, plus the case $S_w = 1.00$, included for comparison. Different line types correspond to different injection flow rates, whereas different line colors correspond to different saturation degrees. Note that, in this regard, we have grouped together $S_w = 0.76$ and $S_w = 0.75$ given their very similar saturation degree. In both panels, the gray shaded areas indicate the range of Q-values associated to vorticity-dominated deformation.

the flow topology (Thiffeault & Finn, 2006). The occurrence of more twisted streamlines evidences the control of topology changes driven by saturation, as described in Figure 4, on the flow field.

Results also show an increase of $\langle |h| \rangle$ with increasing injection flow rate for a given saturation degree. In contrast, this dependency is not linear, given the larger growth rate of $\langle |h| \rangle$ with decreasing S_w for larger q. This trend can be deduced from Equation 4, in which $\vec{v}$ grows linearly, in the same proportion, with q, following the continuity equation. The increment of $\vec{v}$ by a constant scalar function thus results in a linear growth of $\vec{\omega}$ in the same proportion. From the definition of h in Equation 4, this renders the growth of $\langle |h| \rangle$ proportional to the square of the relative increase in q. Note also the narrower range of change in $\langle |h| \rangle$ for the data set corresponding to $S_w = 0.89$ (light blue markers) compared to the remaining cases. This is a consequence of the air clusters volume distribution shown in Figure 3b. Smaller air clusters impose fewer constraints on the flow field, hence causing less streamlines deformation.

4.4. Larger Shear- and Vorticity-Dominated Deformation at Lower Saturation Degree

We now study the interplay between shear and rotational deformation on the local solute plume deformation by employing the Q-criterion (Hunt et al., 1988). We evaluated the scalar field Q expressed in Equation 5, using the computed flow field. This allowed us to identify the regions where $Q > 0$, that is, vorticity-dominated deformation, and those where $Q < 0$, that is, shear-dominated deformation. Figure 6a reports the average of these two ensembles of positive and negative Q-values ($\langle Q \rangle$), respectively, over the entire liquid phase, as a function of saturation, for all tested injection flow rates. As previously explained for the computation of $\langle |h| \rangle$ in Figure 5a, we have included additional cases derived from numerical flow simulations, to obtain an estimate of Q for every experimental S_w at all three experimental q values. Note that we did not explicitly test the minimum pressure condition for every computed Q-value, since the curvature of flow streamlines is implicit in the occurrence of helical flow, as confirmed in Figure 5a.

The results show both a linear increase in the average positive Q-value and a linear decrease in the average negative Q-value with a reduction in saturation, similar to the behavior observed for $\langle |h| \rangle$ (Figure 5a). This indicates that the heterogeneity added by the presence of air in the system increases the magnitude of both shear strain rate and vorticity tensors. However, the increase of negative $\langle Q \rangle$ happens at a faster rate, pointing out a stronger enhancement of the shear strain deformation portion of the local deformation rate tensor. To complement these observations, Figure 6b shows the PDF of Q-values, $p(Q)$, for the experimental cases only, together with the case $S_w = 1.00$. Lower saturation degrees display a broader $p(Q)$, with larger positive and negative values, which

further confirms the behavior observed for $\langle Q \rangle$. $p(Q)$ also depicts a distribution skewed toward negative magnitudes that persists for all S_{w} considered in this work. From the two input variables, S_{w} and q, strong and non-monotonic variations in the skewness were observed only upon varying S_{w}, and not when varying q on the same system (see Figure S8 in Supporting Information S1). Therefore, the system's heterogeneity arising from the presence and distribution of air is the main control on the relative occurrence of shear strain and vorticity-induced deformation. The skewness can even vary largely for very similar saturation degrees, as it occurs for the two cases $S_{\mathrm{w}} = 0.75$ and $S_{\mathrm{w}} = 0.76$. The former case displays a less skewed distribution, indicating that the solute plume deformation is no longer mainly associated to shear-induced stretching, but that more intensive bending is also taking place. This is reflected in the larger deformation of the 50%-concentration isosurface (plume's front deformation) for $S_{\mathrm{w}} = 0.75$ compared to $S_{\mathrm{w}} = 0.76$ in spite of the very similar saturation (see Figure 2b). This interplay between shear-dominated and vorticity-dominated deformation corresponds to the stretching and folding deformation patterns that explain the occurrence of chaotic advection, as observed in previous studies on fully saturated conditions (Heyman et al., 2020; Lester et al., 2013).

Both shear- and vorticity-dominated deformations enhance the growth in time of the interface area between the resident and the injected solution, which contributes to a more efficient mixing through a faster dilution of the solute in the resident liquid phase. Both similar and contrasting mechanisms have been reported at the Darcy scale under fully saturated conditions. On the one side, numerical studies on 2D systems with heterogeneous permeability fields have pointed out the dominant role of shear-dominated regions in controlling solute plume dilution, while vorticity-dominated regions contributed significantly less (de Barros et al., 2012). On the other side, numerical 3D studies on anisotropic porous media have highlighted the role of folding and faster helical motion in enhancing dilution (Chiogna et al., 2016). Our results point out a combined effect of both shear-dominated and vorticity-dominated deformation regions on mixing enhancement. This is characterized by a generally larger contribution from shear, regardless of saturation, and by an increasing importance of vorticity as saturation decreases. These results agree with previous numerical studies at large scale that have shown the combined role of shear- and vorticity-dominated deformation regions on enhanced solute transport dynamics, highlighting the dominant role of pore-scale processes on large-scale observations (Geng et al., 2020). We further emphasize that the relative change in the indexes $\langle |h| \rangle$ and $\langle Q \rangle$ to a given relative change in saturation, as shown in Figures 5a and 6, is not unique, since it ultimately changes with heterogeneity, that is, with the arrangement of material phases in the pore space. This has been shown in the non-unique change of connectivity in the system for very similar saturation degrees (see Figure 4 for $S_{\mathrm{w}} = 0.75$ and $S_{\mathrm{w}} = 0.76$). However, the trends shown here for the change of χ to S_{w}, and for $\langle |h| \rangle$ and $\langle Q \rangle$ as function of S_{w}, are expected to persist for the range of saturation degrees considered in this study. Figure S9 in the Supporting Information S1 further illustrates this point by comparing both $\langle |h| \rangle$ and $\langle Q \rangle$ to changes in χ based on the results plotted in Figures 4–6.

5. Conclusions

Taking advantage of 4D X-ray micro-tomography, performed with very high spatial and temporal resolutions at a synchrotron radiation X-ray imaging beamline, and of an extensive analysis of concentration and velocity vector fields from both the respective experimental data sets and corresponding ones obtained from pore-scale numerical simulations, we have disentangled the mechanisms controlling mixing dynamics in unsaturated porous media under conditions relevant for natural systems. We reveal an enhancement of the mixing efficiency for lower saturation degrees, explained by the development of stronger helical flow. Lower saturation enhances the formation of the backbone of preferential flow via the convergence of different flow paths into preferential channels, resulting in more twisted streamlines, as reflected in a larger helicity density. By Q-criterion computations, we have shown that a lower wetting liquid phase saturation induces an enhancement of both shear- and vorticity-dominated deformation regions, with the former increasing at a faster rate and the latter becoming more relevant at lower saturation. This hints at the interplay between stretching and folding mechanisms (Heyman et al., 2020; Lester et al., 2013), especially at lower saturation degrees, as the main driver of the solute front deformation observed experimentally. Note also the strong impact of slightly unsaturated conditions on the solute front deformation and the mixing presented in this work. Further research will allow considering the effect of saturation degrees below the so-called critical saturation (Raoof & Hassanizadeh, 2013), which are characterized by both a lower dispersivity (Raoof & Hassanizadeh, 2013) and an increasing Euler characteristic (Schlüter et al., 2016) with decreasing S_{w}, on solute's deformation and mixing. We hypothesize contrasting trends to those presented here for such a range, that is, weaker solute's front deformation and less efficient mixing as S_{w}

decreases. Our results also indicate that the flow rate, that is, fluid flow velocity magnitudes, is less relevant in the process of solute plume deformation and therefore a secondary control on mixing.

Solute mixing is relevant in natural and industrial systems, with applications ranging from soil remediation (Burauel & Baßmann, 2005) to chemical reactors (Valdés et al., 2022). Our findings can contribute to the understanding of natural systems and assist in the design of industrial processes. The experimental and numerical framework we present can be a significant starting point to study the control of phase saturation on mixing dynamics with multiphase flow conditions (Berg et al., 2013), that is, with the simultaneous displacement of both immiscible phases. While multiphase flow is expected to enhance mixing because of a new flow phenomenon, the control of phase saturation on mixing, documented and characterized in this study, is expected to persist. In particular, the inter-dependency between wetting and non-wetting phase topology and its variation in time has to be considered when addressing such flow conditions. The possibility to study dynamic processes within the ubiquitous multiphase systems at the relevant spatial and temporal scale using X-ray micro-tomography opens up new research opportunities in further and more realistically studying similar systems under conditions that are very relevant in nature and for a wide spectrum of industrial applications. Aspects, such as temporal resolution, require special consideration and could potentially be further improved compared to the setup presented in this study, for example, by enabling constant sample rotation during image acquisition and/or with the usage of more advanced sample rotation stages, allowing even faster rotation rates. However, for the purpose of vortex identification, the experiment design should consider any eventual additional rotational components to the flow derived from such conditions, demanding the use of rotation invariant vortex identification criteria (Haller, 2005). In addition, newer technical advances could allow for a better compromise between the imaged field of view and the achieved spatial resolution. Moreover, further optimization in the experimental protocol applied in this type of studies would contribute to optimizing beamtime usage, enabling both the accurate acquisition of replicates and the exploration of more experimental conditions (e.g., lower saturation degrees as those presented here). This would enrich the uncertainty quantification on similar data sets and applications. A robust image analysis protocol is also of paramount importance. We are confident that the protocol outlined in this study, and described in detail in the Supporting Information, can find wider application for the correct visualization and segmentation of similar X-ray micro-tomography data sets involving real-time imaging of several material phases and/or a transported solute. Finally, while the porous geometry used in this study provided significant insights on mixing in unsaturated flows, further research on different geometries with additional sources of heterogeneity is still needed to understand the implications of our pore-scale findings on the response of large-scale systems. We believe that the scientific results and the novel experimental applications shown in this study will motivate the further study of similar processes, enriching our understanding of flow and transport in porous systems.

Data Availability Statement

Binary tomographic images of the three material phases (liquid, solid grains, and air) for every single experiment reported in this work are available in Velásquez-Parra et al. (2023), at the Repository for Publications and Research Data of the ETH Zurich.

References

Ali, K., Shah, A. U. H. A., Bilal, S., & Shah, A. U. H. A. (2009). Surface tensions and thermodynamic parameters of surface formation of aqueous salt solutions: III. Aqueous solution of KCl, KBr and KI. *Colloids and Surfaces A: Physicochemical and Engineering Aspects*, *337*(1–3), 194–199. https://doi.org/10.1016/j.colsurfa.2008.12.023

Als-Nielsen, J., & McMorrow, D. (2011). Elements of modern x-ray physics. In *Chap. 1: X-Rays and their interaction with matter* (2nd ed.). John Wiley and Sons, Ltd.

Aref, H., Blake, J. R., Budišić, M., Cardoso, S. S., Cartwright, J. H., Clercx, H. J., et al. (2017). Frontiers of chaotic advection. *Reviews of Modern Physics*, *89*(2), 1–66. https://doi.org/10.1103/RevModPhys.89.025007

Armstrong, R. T., McClure, J. E., Berrill, M. A., Rücker, M., Schlüter, S., & Berg, S. (2016). Beyond Darcy's law: The role of phase topology and ganglion dynamics for two-fluid flow. *Physical Review E*, *94*(4), 1–10. https://doi.org/10.1103/PhysRevE.94.043113

Armstrong, R. T., McClure, J. E., Robins, V., Liu, Z., Arns, C. H., Schlüter, S., & Berg, S. (2019). Porous media characterization using Minkowski functionals: Theories, applications and future directions. *Transport in Porous Media*, *130*(1), 305–335. https://doi.org/10.1007/s11242-018-1201-4

Batchelor, G. K. (2000). *An introduction to fluid dynamics*. Cambridge University Press. https://doi.org/10.1017/CBO9780511800955

Berg, S., Ott, H., Klapp, S. A., Schwing, A., Neiteler, R., Brussee, N., et al. (2013). Real-time 3d imaging of haines jumps in porous media flow. *Proceedings of the National Academy of Sciences of the United States of America*, *110*(10), 3755–3759. https://doi.org/10.1073/pnas.1221373110

Berkowitz, B., Cortis, A., Dentz, M., & Scher, H. (2006). Modeling Non-Fickian transport in geological formations as a continuous time random walk. *Reviews of Geophysics*, *44*(2), 1–49. https://doi.org/10.1029/2005RG000178

Bevington, P. R., & Robinson, D. K. (2003). *Data reduction and error analysis for the physical sciences*. McGraw Hill Higher Education.

Blasquez, I., & Poiraudeau, J. (2003). Efficient processing of Minkowski functionals on a 3D binary image using binary decision diagrams. *Journal of WSCG*, *11*(1–3). Retrieved from hdl.handle.net/11025/1669[

Boon, M., Bijeljic, B., & Krevor, S. (2017). Observations of the impact of rock heterogeneity on solute spreading and mixing. *Water Resources Research*, *53*(6), 4624–4642. https://doi.org/10.1002/2016WR019912

Bordoloi, A. D., Scheidweiler, D., Dentz, M., Bouabdellaoui, M., Abbarchi, M., & de Anna, P. (2022). Structure induced laminar vortices control anomalous dispersion in porous media. *Nature Communications*, *13*(1), 3820. https://doi.org/10.1038/s41467-022-31552-5

Buades, A., Coll, B., & Morel, J. M. (2005). A review of image denoising algorithms, with a new one. *Multiscale Modeling and Simulation*, *4*(2), 490–530. https://doi.org/10.1137/040616024

Bührer, M., Stampanoni, M., Rochet, X., Büchi, F., Eller, J., & Marone, F. (2019). High-numerical-aperture macroscope optics for time-resolved experiments. *Journal of Synchrotron Radiation*, *26*(4), 1161–1172. https://doi.org/10.1107/S1600577519004119

Burauel, P., & Baßmann, F. (2005). Soils as filter and buffer for pesticides—Experimental concepts to understand soil functions. *Environmental Pollution*, *133*(1), 11–16. https://doi.org/10.1016/j.envpol.2004.04.011

Chen, Y., Steeb, H., Erfani, H., Karadimitriou, N. K., Walczak, M. S., Ruf, M., et al. (2021). Nonuniqueness of hydrodynamic dispersion revealed using fast 4D synchrotron x-ray imaging. *Science Advances*, *7*(52), 1–7. https://doi.org/10.1126/sciadv.abj0960

Chiogna, G., Cirpka, O. A., & Herrera, P. A. (2016). Helical flow and transient solute dilution in porous media. *Transport in Porous Media*, *111*(3), 591–603. https://doi.org/10.1007/s11242-015-0613-7

Chiogna, G., Rolle, M., Bellin, A., & Cirpka, O. A. (2014). Helicity and flow topology in three-dimensional anisotropic porous media. *Advances in Water Resources*, *73*, 134–143. https://doi.org/10.1016/j.advwatres.2014.06.017

Danckwerts, P. V. (1952). The definition and measurement of some characteristics of mixtures. *Applied Scientific Research*, *3*(4), 279–296. https://doi.org/10.1007/bf03184936

Datta, S. S., Chiang, H., Ramakrishnan, T. S., & Weitz, D. A. (2013). Spatial fluctuations of fluid velocities in flow through a three-dimensional porous medium. *Physical Review Letters*, *111*(6), 1–5. https://doi.org/10.1103/PhysRevLett.111.064501

de Anna, P., Jimenez-Martinez, J., Tabuteau, H., Turuban, R., Le Borgne, T., Derrien, M., & Meheust, Y. (2014). Mixing and reaction kinetics in porous media: An experimental pore scale quantification. *Environmental Science and Technology*, *48*(1), 508–516. https://doi.org/10.1021/es403105b

de Anna, P., Le Borgne, T., Dentz, M., Tartakovsky, A. M., Bolster, D., & Davy, P. (2013). Flow intermittency, dispersion, and correlated continuous time random walks in porous media. *Physical Review Letters*, *110*(18), 1–5. https://doi.org/10.1103/PhysRevLett.110.184502

de Anna, P., Quaife, B., Biros, G., & Juanes, R. (2017). Prediction of the low-velocity distribution from the pore structure in simple porous media. *Physical Review Fluids*, *2*(12), 124103. https://doi.org/10.1103/PhysRevFluids.2.124103

de Barros, F. P., Dentz, M., Koch, J., & Nowak, W. (2012). Flow topology and scalar mixing in spatially heterogeneous flow fields. *Geophysical Research Letters*, *39*(8), 1–5. https://doi.org/10.1029/2012GL051302

De Chaumont, F., Dallongeville, S., Chenouard, N., Hervé, N., Pop, S., Provoost, T., et al. (2012a). Icy: An open bioimage informatics platform for extended reproducible research. *Nature Methods*, *9*(7), 690–696. https://doi.org/10.1038/nmeth.2075

De Chaumont, F., Dallongeville, S., Chenouard, N., Hervé, N., Pop, S., Provoost, T., et al. (2012b). Icy: An open bioimage informatics platform for extended reproducible research. Version 2.1.3.0 [Software]. https://icy.bioimageanalysis.org/

De Gennes, P. G. (1983). Hydrodynamic dispersion in unsaturated porous media. *Journal of Fluid Mechanics*, *136*(-1), 189–200. https://doi.org/10.1007/978-1-4757-2558-2_2

Dentz, M., Hidalgo, J. J., & Lester, D. (2022). Mixing in porous media: Concepts and approaches across scales. *Transport in Porous Media*, *146*(1–2), 5–53. https://doi.org/10.1007/s11242-022-01852-x

Dentz, M., Le Borgne, T., Englert, A., & Bijeljic, B. (2011). Mixing, spreading and reaction in heterogeneous media: A brief review. *Journal of Contaminant Hydrology*, *120*, 1–17. https://doi.org/10.1016/j.jconhyd.2010.05.002

Desnoyers, J. E., & Perron, G. (1972). The viscosity of aqueous solutions of alkali and tetraalkylammonium halides at 25°C. *Journal of Solution Chemistry*, *1*(3), 199–212. https://doi.org/10.1007/BF00645101

Dobson, K. J., Coban, S. B., McDonald, S. A., Walsh, J. N., Atwood, R. C., & Withers, P. J. (2016). 4-D imaging of sub-second dynamics in pore-scale processes using real-time synchrotron X-ray tomography. *Solid Earth*, *7*(4), 1059–1073. https://doi.org/10.5194/se-7-1059-2016

Dunlop, P. J., & Stokes, R. H. (1951). The diffusion coefficients of Sodium and Potassium iodides in aqueous solution at 25 C. *Journal of the American Chemical Society*, *73*(11), 5456–5457. https://doi.org/10.1021/ja01155a521

Geng, X., Michael, H. A., Boufadel, M. C., Molz, F. J., Gerges, F., & Lee, K. (2020). Heterogeneity affects intertidal flow topology in coastal beach aquifers. *Geophysical Research Letters*, *47*(17), 1–12. https://doi.org/10.1029/2020GL089612

Guédon, G. R., Inzoli, F., Riva, M., & Guadagnini, A. (2019). Pore-scale velocities in three-dimensional porous materials with trapped immiscible fluid. *Physical Review E*, *100*(4), 043101. https://doi.org/10.1103/physreve.100.043101

Haller, G. (2005). An objective definition of a vortex. *Journal of Fluid Mechanics*, *525*, 1–26. https://doi.org/10.1017/S0022112004002526

Hasan, S., Joekar-Niasar, V., Karadimitriou, N. K., & Sahimi, M. (2019). Saturation dependence of non-fickian transport in porous media. *Water Resources Research*, *55*(2), 1153–1166. https://doi.org/10.1029/2018WR023554

Hasan, S., Niasar, V., Karadimitriou, N. K., Godinho, J. R., Vo, N. T., An, S., et al. (2020). Direct characterization of solute transport in unsaturated porous media using fast X-ray synchrotron microtomography. *Proceedings of the National Academy of Sciences of the United States of America*, *117*(38), 23443–23449. https://doi.org/10.1073/pnas.2011716117

Heyman, J., Lester, D. R., Turuban, R., Méheust, Y., & Le Borgne, T. (2020). Stretching and folding sustain microscale chemical gradients in porous media. *Proceedings of the National Academy of Sciences of the United States of America*, *117*(24), 13359–13365. https://doi.org/10.1073/pnas.2002858117

Hu, Y., Schneider, T., Wang, B., Zorin, D., & Panozzo, D. (2020). Fast tetrahedral meshing in the wild. *ACM Transactions on Graphics*, *39*(4). https://doi.org/10.1145/3386569.3392385

Hunt, J., Wray, A., & Moin, P. (1988). Eddies, streams, and convergence zones in turbulent flows. In *Center for turbulence research, proceedings of the summer program* (pp. 193–208).

Jha, B., Cueto-Felgueroso, L., & Juanes, R. (2011). Fluid mixing from viscous fingering. *Physical Review Letters*, *106*(19), 194502. https://doi.org/10.1103/PhysRevLett.106.194502

Jiménez-Martínez, J., de Anna, P., Tabuteau, H., Turuban, R., Le Borgne, T., & Méheust, Y. (2015). Pore-scale mechanisms for the enhancement of mixing in unsaturated porous media and implications for chemical reactions. *Geophysical Research Letters*, *42*(13), 5316–5324. https://doi.org/10.1002/2015GL064513

Jiménez-Martínez, J., Le Borgne, T., Tabuteau, H., & Méheust, Y. (2017). Impact of saturation on dispersion and mixing in porous media: Photobleaching pulse injection experiments and shear-enhanced mixing model. *Water Resources Research*, *53*(2), 1457–1472. https://doi.org/10.1002/2016WR019849

Kang, P. K., de Anna, P., Nunes, J. P., Bijeljic, B., Blunt, M. J., & Juanes, R. (2014). Pore-scale intermittent velocity structure underpinning anomalous transport through 3-D porous media. *Geophysical Research Letters*, *41*(17), 6184–6190. https://doi.org/10.1002/2014GL061475

Karadimitriou, N. K., Joekar-Niasar, V., Babaei, M., & Shore, C. A. (2016). Critical role of the immobile zone in non-Fickian two-phase transport: A new paradigm. *Environmental Science and Technology*, *50*(8), 4384–4392. https://doi.org/10.1021/acs.est.5b05947

Kitanidis, K. (1994). The concept of the dilution index. *Water Resources Research*, *30*(7), 2011–2026. https://doi.org/10.1029/94wr00762

Kitware, I. (2023). Paraview. Version: 5.10.0 [Software]. https://www.paraview.org/

Lasseux, D., Valdés-Parada, F., & Wood, B. (2021). Recent developments in upscaling and characterization of flow and transport in porous media. *Advances in Water Resources*, *150*, 1–5. https://doi.org/10.1016/j.advwatres.2021.103886

Lavin, A., De Vicente, J., Holgado, M., Laguna, M. F., Casquel, R., Santamaria, B., et al. (2018). On the determination of uncertainty and limit of detection in label-free biosensors. *Sensors*, *18*(38), 2038. https://doi.org/10.3390/s18072038

Lehoux, A. P., Rodts, S., Faure, P., Michel, E., Courtier-Murias, D., & Coussot, P. (2016). Magnetic resonance imaging measurements evidence weak dispersion in homogeneous porous media. *Physical Review E*, *94*(5), 053107. https://doi.org/10.1103/physreve.94.053107

Lester, D. R., Metcalfe, G., & Trefry, M. G. (2013). Is chaotic advection inherent to porous media flow? *Physical Review Letters*, *111*(17), 174101. https://doi.org/10.1103/PhysRevLett.111.174101

Lester, D. R., Trefry, M. G., & Metcalfe, G. (2016). Chaotic advection at the pore scale: Mechanisms, upscaling and implications for macroscopic transport. *Advances in Water Resources*, *97*, 175–192. https://doi.org/10.1016/j.advwatres.2016.09.007

Levy, M., & Berkowitz, B. (2003). Measurement and analysis of non-Fickian dispersion in heterogeneous porous media. *Journal of Contaminant Hydrology*, *64*(3–4), 203–226. https://doi.org/10.1016/S0169-7722(02)00204-8

Li, L., Maher, K., Navarre-Sitchler, A., Druhan, J., Meile, C., Lawrence, C., et al. (2017). Expanding the role of reactive transport models in critical zone processes. *Earth-Science Reviews*, *165*, 280–301. https://doi.org/10.1016/j.earscirev.2016.09.001

Lloyd, S. (1982). Least squares quantization in PCM. *IEEE Transactions on Information Theory*, *28*(2), 129–137. https://doi.org/10.1109/TIT.1982.1056489

Markale, I., Cimmarusti, G. M., Britton, M. M., & Jiménez-Martínez, J. (2021). Phase saturation control on mixing-driven reactions in 3D porous media. *Environmental Science and Technology*, *55*(13), 8742–8752. https://doi.org/10.1021/acs.est.1c01288

Marone, F., Schlepütz, C. M., Marti, S., Fusseis, F., Velásquez-Parra, A., Griffa, M., et al. (2020). Time resolved in situ X-Ray tomographic microscopy unraveling dynamic processes in geologic systems. *Frontiers in Earth Science*, *7*, 1–20. https://doi.org/10.3389/feart.2019.00346

Marone, F., & Stampanoni, M. (2012). Regridding reconstruction algorithm for real-time tomographic imaging. *Journal of Synchrotron Radiation*, *19*(6), 1029–1037. https://doi.org/10.1107/S0909049512032864

Michielsen, K., & De Raedt, H. (2001). Integral-geometry morphological image analysis. *Physics Reports*, *347*(6), 461–538. https://doi.org/10.1016/S0370-1573(00)00106-X

Moffatt, H. K., & Tsinober, A. (1992). Helicity in laminar and turbulent flow. *Annual Review of Fluid Mechanics*, *24*(1), 281–312. https://doi.org/10.1146/annurev.fl.24.010192.001433

Münch, B. (2022). Xlib library of ImageJ plugins [Software]. Retrieved from https://imagej.net/plugins/xlib/

Okubo, A. (1970). Horizontal dispersion of floatable particles in the vicinity of velocity singularities such as convergences. *Deep-Sea Research and Oceanographic Abstracts*, *17*(3), 445–454. https://doi.org/10.1016/0011-7471(70)90059-8

Ottino, J. M. (1989). *The kinematics of mixing: Stretching, chaos, and transport*. Cambridge University Press.

Paganin, D., Mayo, S. C., Gureyev, T. E., Miller, P. R., & Wilkins, S. W. (2002). Simultaneous phase and amplitude extraction from a single defocused image of a homogeneous object. *Journal of Microscopy*, *206*(1), 33–40. https://doi.org/10.1046/j.1365-2818.2002.01010.x

Puyguiraud, A., Gouze, P., & Dentz, M. (2021). Pore-scale mixing and the evolution of hydrodynamic dispersion in porous media. *Physical Review Letters*, *126*(16), 164501. https://doi.org/10.1103/PhysRevLett.126.164501

Raoof, A., & Hassanizadeh, S. M. (2013). Saturation-dependent solute dispersivity in porous media: Pore-scale processes. *Water Resources Research*, *49*(4), 1943–1951. https://doi.org/10.1002/wrcr.20152

Schlüter, S., Berg, S., Rücker, M., Armstrong, R. T., Vogel, H.-J., Hilfer, R., & Wildenschild, D. (2016). Pore-scale displacement mechanisms as a source of hysteresis for two-phase flow in porous media. *Water Resources Research*, *52*(3), 2194–2205. https://doi.org/10.1002/2015WR018254

Schneider, C. A., Rasband, W. S., & Eliceiri, K. W. (2012a). ImageJ. Version: 2.3.051 [Software]. https://imagej.net/

Schneider, C. A., Rasband, W. S., & Eliceiri, K. W. (2012b). NIH image to ImageJ: 25 years of image analysis. *Nature Methods*, *9*(7), 671–675. https://doi.org/10.1038/nmeth.2089

Shih, Y. H., Hsu, S. Y., Huang, Q. Z., Lamorski, K., Hu, M. C., Tsao, C. W., et al. (2022). Euler characteristic during drying of porous media. *Drying Technology*, *40*(4), 781–795. https://doi.org/10.1080/07373937.2021.2007946

Simunek, J., van Genuchten, M. T., & Sejna, M. (2008). Development and applications of the hydrus and stanmod software packages and related codes. *Vadose Zone Journal*, *7*(2), 587–600. https://doi.org/10.2136/vzj2007.0077

Souzy, M., Lhuissier, H., Méheust, Y., Le Borgne, T., & Metzger, B. (2020). Velocity distributions, dispersion and stretching in three-dimensional porous media. *Journal of Fluid Mechanics*, *891*, A16. https://doi.org/10.1017/jfm.2020.113

Sposito, G. (2001). Topological groundwater hydrodynamics. *Advances in Water Resources*, *24*(7), 793–801. https://doi.org/10.1016/S0309-1708(00)00077-4

Szulczewski, M. L., MacMinn, C. W., Herzog, H. J., & Juanes, R. (2012). Lifetime of carbon capture and storage as a climate-change mitigation technology. *Proceedings of the National Academy of Sciences of the United States of America*, *109*(14), 5185–5189. https://doi.org/10.1073/pnas.1115347109

Tallakstad, K. T., Knudsen, H. A., Ramstad, T., Løvoll, G., Måløy, K. J., Toussaint, R., & Flekkøy, E. G. (2009). Steady-state two-phase flow in porous media: Statistics and transport properties. *Physical Review Letters*, *102*(7), 074502. https://doi.org/10.1103/PhysRevLett.102.074502

Tallakstad, K. T., Løvoll, G., Knudsen, H. A., Ramstad, T., Flekkøy, E. G., & Måløy, K. J. (2009). Steady-state, simultaneous two-phase flow in porous media: An experimental study. *Physical Review E*, *80*(3), 1–13. https://doi.org/10.1103/PhysRevE.80.036308

Tang, J., Smit, M., Vincent-Bonnieu, S., & Rossen, W. R. (2019). New capillary number definition for micromodels: The impact of pore microstructure. *Water Resources Research*, *55*(2), 1167–1178. https://doi.org/10.1029/2018WR023429

The MathWorks, I. (2022). *Matlab version: 9.13.0 (r2022b)*. The MathWorks Inc. Retrieved from https://www.mathworks.com

ThermoFisher Scientific, I. (2022). Avizo. Retrieved from https://www.thermofisher.com/ch/en/home/electron-microscopy/products/software-em-3d-vis/avizo-software.html

Thiffeault, J. L., & Finn, M. D. (2006). Topology, braids and mixing in fluids. *Philosophical Transactions of the Royal Society A: Mathematical, Physical & Engineering Sciences*, *364*(1849), 3251–3266. https://doi.org/10.1098/rsta.2006.1899

Triadis, D., Jiang, F., & Bolster, D. (2019). Anomalous dispersion in pore-scale simulations of two-phase flow. *Transport in Porous Media*, *126*(2), 337–353. https://doi.org/10.1007/s11242-018-1155-6

Valdés, J. P., Kahouadji, L., & Matar, O. K. (2022). Current advances in liquid–liquid mixing in static mixers: A review. *Chemical Engineering Research and Design*, *177*, 694–731. https://doi.org/10.1016/j.cherd.2021.11.016

Velásquez-Parra, A., Aquino, T., Willmann, M., Méheust, Y., Le Borgne, T., & Jiménez-Martínez, J. (2022). Sharp transition to strongly anomalous transport in unsaturated porous media. *Geophysical Research Letters*, *49*(3), 1–10. https://doi.org/10.1029/2021gl096280

Velásquez-Parra, A., Marone, F., Kaufmann, R., Griffa, M., & Jiménez-Martínez, J. (2023). Synchrotron X-ray micro-tomography of single material phases in an unsaturated porous medium [Dataset]. ETH Zürich Research Collection. https://doi.org/10.3929/ethz-b-000645503

Vogel, H.-J. (2002). Topological characterization of porous media. In K. Mecke & D. Stoyan (Eds.), *Morphology of condensed matter. Physical and geometry of spatially complex systems*. Springer.

Weiss, J. (1991). The dynamics of enstrophy transfer in two-dimensional hydrodynamics. *Physica D: Nonlinear Phenomena*, *48*(2–3), 273–294. https://doi.org/10.1016/0167-2789(91)90088-Q

Xu, R., Prodanović, M., & Landry, C. (2020). Pore-scale study of water adsorption and subsequent methane transport in clay in the presence of wettability heterogeneity. *Water Resources Research*, *56*(10), 1–15. https://doi.org/10.1029/2020WR027568

Yu, Y., Chiogna, G., Cirpka, O. A., Grathwohl, P., & Rolle, M. (2015). Experimental evidence of helical flow in porous media. *Physical Review Letters*, *115*(19), 194502. https://doi.org/10.1103/PhysRevLett.115.194502